Published in final edited form as:

Chemistry. 2015 September 14; 21(38): 13420–13430. doi:10.1002/chem.201501104.

Molecular Mixed–Metal Manganese Oxido Cubanes as Precursors to Heterogeneous Oxygen Evolution Catalysts

Sandy Suseno[a], **Dr. Charles C. L. McCrory**[b], **Dr. Rosalie Tran**[c], **Dr. Sheraz Gul**[c], **Dr. Junko Yano**[c], and **Prof. Theodor Agapie**[a]

Theodor Agapie: agapie@caltech.edu

[a]Division of Chemistry and Chemical Engineering, California Institute of Technology, 1200 East California Boulevard, MC 127-72, Pasadena, California 91125, United States

[b]Joint Center for Artificial Photosynthesis, Pasadena, California 91125, United States

[c]Physical Biosciences Division, Lawrence Berkeley National Laboratory, Berkeley, California 94720, United States

Abstract

Well-defined mixed–metal [$CoMn_3O_4$] and [$NiMn_3O_4$] cubane complexes were synthesized and used as precursors for heterogeneous oxygen evolution reaction (OER) electrocatalysts. The discrete clusters were dropcasted onto glassy carbon (GC) and indium-tin oxide (ITO) electrodes, and the OER activities of the resulting films were evaluated. The catalytic surfaces were analysed by various techniques to gain insight into the structure-function relationships of the electrocatalysts' heterometallic composition. Depending on preparation conditions, the Co-Mn-oxide was found to change metal composition during catalysis, while the Ni-Mn-oxides maintained the $NiMn_3$ ratio. XAS studies provided structural insights indicating that the electrocatalysts are different from the molecular precursors, but that the original $NiMn_3O_4$ cubane-like geometry was maintained in the absence of thermal treatment (**2-Ni**). In contrast, the thermally generated **3-Ni** develops an oxide-like extended structure. Both **2-Ni** and **3-Ni** show structural changes upon electrolysis, but they do not convert to the same material. The observed structural motifs in these heterogeneous electrocatalysts are reminiscent of the biological Oxygen Evolving Complex in Photosystem II, including the MMn_3O_4 cubane moiety. The reported studies demonstrate the use of discrete heterometallic-oxide clusters as precursors for heterogeneous water oxidation catalysts of novel composition and the distinct behavior of two sets of mixed-metal oxides.

Graphical Abstract

Correspondence to: Junko Yano; Theodor Agapie, agapie@caltech.edu.

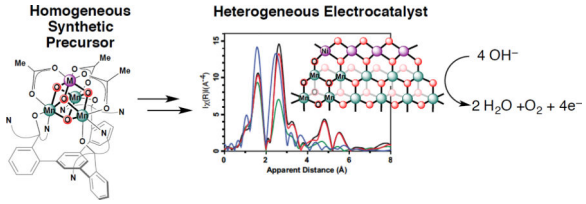

Keywords

oxygen evolution reaction; electrocatalyst; manganese oxide; cubane; synthetic precursor

Introduction

Metal oxides have been extensively studied as electrocatalysts for the oxidation of water in the oxygen evolution reaction (OER, Eq. 1).[1] Typically, metal oxide films are obtained through precipitation, anodic electrodeposition or adsorption/deposition onto the support materials (Fe, Co, Ni, Ir, Ru, Mn).[2]

$$2H_2O \rightarrow O_2 + 4H^+ + 4e^- \quad \text{(Eq. 1)}$$

The detailed mechanism for the formation of the O–O bond is still under debate although several mechanistic pathways have been proposed.[1a, 3] A general mechanism for the OER on metal oxides involves water coordination to the surface active site followed by a proton transfer to the solvent and an electron transfer to the electrode to form a surface M–OH species. Subsequently, a metal-oxo species is generated via proton-coupled oxidation or disproportionation of two M–OH species to lose H_2O. Generation of O_2 is proposed via reaction of two metal-oxo moieties or by attack of water or hydroxide on a metal-oxo moiety. Despite the lack of full mechanistic insight into this transformation, all proposals suggest the importance of the M–OH intermediates, and subsequently, the M–O bond in the OER electrocatalytic activity. OER activity has been shown to linearly correlate to the standard enthalpy of formation of the corresponding $M(OH)_3$ for late first-row transition metal perovskites.[4] O_2 evolution has been proposed to follow metal oxide redox transitions as shown by a linear correlation between the minimum potential required for OER and the catalysts' lower oxide/higher oxide redox potentials.[5] A "volcano plot" relates the OER activity to the M–O bond strength by correlating the overpotential of certain metal oxides at a fixed current density to the enthalpy of a lower-to-higher oxide transition.[6] With these mechanistic proposals for homometallic oxides, mixed-metal oxides with weaker M–O bonds are expected to display enhanced OER behavior.

The OER activity of mixed metal oxides especially in spinels has been examined to determine the heterometallic effect relative to each homometallic oxides.[4, 7] The enhanced activity has been proposed to be correlated to the changes in the enthalpy of the metal-oxide oxidation state transition[8] and work function upon metal atom substitution.[7a] Some of the mixed metal oxides that have shown enhanced OER activity are Ni–Fe,[9] Ni–Co,[9k, 10a, 10b] Ni–Cu,[9k, 11] Co–Fe,[9k, 12] Co–Mo,[13] Fe–Mo,[14] Cu–Co,[15] and Mn–M.[2d, 16] Mixed-

oxides of three or more metal combinations such as Co–Cr–Fe[17] and Ni-Fe-M have also been reported as OER electrocatalysts with enhanced activity.[9k, 18]

The preparation of mixed metal oxide material with controlled metal-to-metal stoichiometry has been challenging as binary metal oxide films typically have bulk- and surface-metal compositions that differ from the stoichiometry of the precursor solutions.[9c, 16a, 19] Recently, a photochemical metal-organic deposition method has been reported as a facile technique for preparing amorphous phases of mixed metal oxides with controlled stoichiometry and high OER electrocatalytic activity.[20] While many metal-oxides have been reported for OER, composition-function relationships of heterometallic oxides have been less-extensively studied, in part due to challenges in preparing controlled composition and structure.[7a, 9c, 16a, 21]

Molecular multimetallic complexes have been shown to serve as precursors to heterogeneous or supported OER catalysts.[2j, 22] Employing well-defined heterometallic clusters as precursors is a potential strategy for maintaining metal stoichiometry and relative metal arrangement in the resulting heterogeneous OER catalysts. Herein, we employ discrete synthetic cluster precursors for the synthesis of bimetallic oxides active for electrolytic water oxidation. The effect of the preparation method and type of precursor on the composition, structure, and electrocatalytic performance of the heterogeneous oxide is evaluated. Maintaining of the ratio of two metals during electrolysis is dependent on the nature of the components.

Results and Discussion

We have recently developed synthetic protocol for the synthesis of heterometallic manganese oxido cubane clusters [MMn_3O_4] that display redox active metals M (Scheme 1; **1-M**, M = Fe^{3+}, Co^{3+}, Ni^{2+}, Cu^{2+}) via transmetallation from **1-Ca**. These are structurally analogous to the previously investigated complexes (where M = Ca^{2+}, Sr^{2+}, Zn^{2+}, Y^{3+}, Sc^{3+}, Mn^{3+}).[23] These clusters serve as precursors to ternary metal oxides of controlled M:Mn ratio of 1:3. The catalytically active metal oxide films were prepared by dropcasting solutions of **1-M** (M = Co, Ni) in dimethylformamide (DMF) onto the surface of indium tin oxide (ITO) on glass substrates or glassy carbon (GC) disk electrodes (Scheme 1). Removal of solvent *in vacuo* yielded a thick layer of film, **2-M** that was treated to generate the catalyst (Scheme 1). Another protocol used to prepare a different material **3-M** involves heating the dried film **2-M** to remove the organic ligands (L and acetates) from the metal-oxido core (Scheme 1).

The electrochemical behavior of the materials **2-M** and **3-M** were studied in basic aqueous media, and the steady-state current densities (*j*) as a function of the overpotential (η) were recorded to probe the kinetics of the reaction. Upon electrolysis in basic media (pH 13 or 14) and release of gas, the top layer of the dropcasted film **2** was observed to fall into solution, producing the catalytically active thin layer (< 200 μm) on the electrode.

Rotating disk voltammetry (RDV) measurements, chronopotentiometry (CP), and chronoamperometry (CA) studies all at 1600 rpm were performed to investigate the activity of the resulting surface material before and after 2 h electrolysis (t_{CP} = 0 and 2 h; Figure 1a–

c) by evaluating the overpotential required to achieve current densities of 10 mA cm^{-2} ($\eta_{j=10\ mA\ cm-2}$) as the metric relevant for solar fuel synthesis.[7a] In addition, the current density of each catalyst on ITO was measured as a function of the overpotential (Tafel plot) in static solutions of 0.1 M KOH (Figure 2) from cyclic voltammetry (CV) measurements. The corresponding Tafel slopes, $\eta_{j=10\ mA\ cm-2}$ values from RDV studies, and the overpotentials required to achieve current densities of 1 mA cm^{-2} from static CV measurements are shown in Table 1.

The elemental compositions of the **2-M** and **3-M** were determined by X-ray photoelectron spectroscopy (XPS), energy dispersive X-ray spectroscopy (EDS), and inductively coupled plasma mass spectrometry (ICP–MS). The results from the three techniques are summarized in Table 2.

Prior to electrolysis, the dropcasted films **2-Co** and **2-Ni** show M to Mn ratio of ~1:3 based on XPS and EDS (only XPS data are shown in Table 1 for this series) consistent with ratio in the molecular precursors **1-Co** and **1-Ni**. The elemental composition analyses of the resulting metal oxide films *after* electrolysis (1–5 h of CP) show retention of the ~1:3 M to Mn ratio for all **2-Ni**, **3-Co**, and **3-Ni**, but resulted in lower average Co:Mn ratio of 1 to 1.2 for **2-Co** (Table 2). Both **2-Co** and **2-Ni** films after electrolysis and **3-Co** and **3-Ni** films do not display any N 1s peak by XPS, indicating the loss of ligand L upon electrolysis and heat treatment, respectively. This is supported by the thermogravimetric analysis of **1-Co** (Figure S1 in Supporting Info) where the loss of ~77% mass was observed upon heating at 400 °C for 4 h, consistent with calculated mass loss of all ligands (acetates and L) at ~78%. ICP-MS studies were performed only on the resulting materials after electrolysis of **2-M** on the GC disks to avoid signal saturation by ITO.

Scanning electron microscopy (SEM) was used to characterize the surface morphologies for all metal oxide films **2** and **3** (Figure 3). The initial surface of the dropcasted material (in this case **1-Co**) is shown in Figure 3a as thick amorphous layer on the ITO electrode. Upon water electrolysis (CP at 5 mA cm^{-2}) with this material for 5 h, the resulting material consists of a very thin electroactive metal oxide layer represented by Figure 3c. Figure 3b and 3d show the resulting thermally treated electroactive layer of **3-Co** and **3-Ni** respectively before and after electrolysis, where no obvious change on the surface morphology was observed. Figure 3e, f display the crystalline-looking final thin layer film of **2-Ni** after electrolysis from the top view and the cross-section respectively. In addition to SEM, elemental mapping of the surfaces was also performed. The elemental maps of **3-Ni** and **2-Co** on ITO electrode are displayed in Figure 4. The elemental map reveals the uniformly scattered presence of Ni and Mn in the heterogeneous material. This observation is in contrast to the Co-containing materials where Co was detected throughout the surface while the presence of Mn was more localized on the “island” (Figure 4). Powder X-ray diffraction studies of these surfaces show no other patterns from those resulting from the background ITO electrode (see Supporting Info. Figure S5), indicative that they are either amorphous or possibly too thin with ~2 μm thickness (Figure 3f) for detection.

RDV and CP studies of **2-Co** show similar activity at t_{CP} = 0 h vs. 2 h (Figure 1a,c). On the other hand, the electrochemical studies on **2-Ni** film indicate that the initial film has low

electrocatalytic activity for OER, but possibly structurally rearranged upon electrolysis to generate a more active material with improved overpotential to produce 10 mA cm^{-2} current density (Figure 1b, c). The **3-Co** and **3-Ni** films retain similar electrocatalytic activity throughout electrolysis period (Figure S2–S3 in Supporting Info.). The observed overpotentials (0.36 – 0.43 V) to reach 1 mA cm^{-2} current density for **2** and **3** (Figure 2, Table 1) as a measure of electrocatalytic activity are comparable to a number of other homo- and heterometallic oxide electrocatalysts.[2a–c, 2f, 9h, 9i]

In addition, RDV studies of **2-Co** and **2-Ni** on GC electrodes resulted in $\eta_{j=10\ mA\ cm-2}$ values and electrochemically active surface area (ECSA) that are comparable to other selected reported metal oxide films under identical conditions (Table 3).[9k] This suggests that both activity per geometric area and the specific activity per ECSA of **2-Co** and **2-Ni** are similar to other catalytic materials electrodeposited deposits from metal salts. The amount of O_2 produced by **2-Co** and **2-Ni** throughout 2h constant current electrolyses at 1 mA cm^{-2} was quantified using a fluorescent oxygen sensor and suggests nearly 100% Faradaic efficiency for the electrocatalytic process. These results indicate that the synthetic cubane complexes **1-M** (M = Co, Ni) can serve as precursors to generate competent and selective OER electrocatalysts with applied oxidative potentials.

Further investigations of the final metal compositions of these electrocatalysts were performed to complement the results from the electrochemical studies. Material **2-Co** was observed to undergo the largest variation in M to Mn stoichiometry before vs. after 1–5 h electrolysis (Table 2). While the reported value in Table 2 is an average of all analyzed spots on the non-uniform electrode surface, there were multiple areas on the electrode evaluated by XPS and EDS that display Co : Mn ratio of 1 to ~0.1; the Co $2p_{3/2}$ peak was primarily the only metal signal observed in the spectrum. This result suggests that most of the Mn centers dissolved in the solution during electrocatalytic oxidation of hydroxide ions to O_2, likely via reduced metal species (Mn^{II} and Mn^{III}) that are soluble in water and kinetically labile. The generated catalyst, a predominantly the homometallic cobalt oxide (CoO_x) film, remains active for water oxidation.

The elemental analyses data for **2-Ni**, **3-Co**, and **3-Ni** display retention of the metal stoichiometry even after prolonged electrolysis periods, providing evidence that the cluster cores may have stayed intact in those films, or that they have converted to materials that maintain the 3:1 Mn:M ratio. Additionally, elemental mapping of the surfaces of **2-Ni**, **3-Co**, and **3-Ni** (Figure 4 and Supporting Info.) *after* electrolysis show no obvious phase separation of M and Mn, suggesting the retention and co-localization of both metals in the electrocatalysts. On the other hand, the elemental map of **2-Co** *after* electrolysis shows variable distribution of Co and Mn on the larger island piece vs. the rest of the surface (Figure 4), consistent with the non-uniform electrodeposition of Co back onto the electrode throughout electrolysis. Further studies are required to determine whether structural rearrangements may have occurred or the electrodeposition of the dissociated M^{II} salts back onto the electrode favors similar 1:3 M to Mn metal stoichiometry. Based on the elemental composition studies, **1-Co** and **1-Ni** can indeed serve as precursors to catalytically active materials for OER with control over M : Mn ratio for **2-Ni**, **3-Co**, and **3-Ni**. This demonstration suggests that the structure and composition of mixed-metal catalysts can be

tuned by the selection of heterometallic molecular precursors. The variation in composition of **2-Co** highlights the importance of thoroughly evaluating the compositions of metal oxide materials pre- and post-catalysis, especially for those heterometallic oxides that were not prepared via electrodeposition method.

The Ni-Mn OER catalysts maintain the metal ratio despite being prepared under different conditions. However, the variation in catalytic properties of **2-Ni** suggests that structural changes may occur during catalysis. X-ray absorption spectroscopic (XAS) studies were performed to determine whether the metal oxides underwent structural changes/ rearrangements during electrocatalysis. Figures 5 and 6 show the Mn and Ni XANES (X-ray Near Edge Structure) and EXAFS (Extended X-ray Absorption Fine Structure) spectra of **2-Ni** at t_{CP} = 1 and 5 h and **3-Ni** at t_{CP} = 0, 1, and 5 h together with those of the dropcasted complex **1-Ni**. The EXAFS curve fitting results of the selected samples are shown in the SI (Figure S18).

Both Mn and Ni data suggest that the Mn and Ni local environment of the dropcasted **1-Ni** was altered during the electrolysis (**2-Ni**) (Figures 5a,b and 6a,b) and more significantly by the heat treatment (**3-Ni**) (Figures 5c,d and 6c,d). While the Mn and Ni XANES edge positions of **2-Ni** are close to those of **1-Ni** and the EXAFS peak positions are essentially the same as those of **1-Ni**, a significant reduction of the EXAFS peak intensity is observed (Figure 6a,b). This indicates the larger distribution of metal-ligand and metal-metal distances compared to the original **1-Ni** structure, and its effect is reflected in the larger Debye-Waller factors (s^2) of the metal-metal interactions in the EXAFS fit parameters of both Mn and Ni in **2-Ni** (see Table S1 and S2 in Supporting Info). There are no detectable peaks above the noise level in the long range (apparent distances in the range of 4 to 6 Å in Figure 6a,b) of **2-Ni**, suggesting no formation of the extended oxide-like structure at this stage. This indicates the retention of the basic cubane-core structure during electrolysis.

When the dropcasted **1-Ni** is heat-treated (**3-Ni**), the Mn XANES rising edge positions are shifted to lower energy, suggesting the reduction of Mn from Mn^{IV} (Figure 5c). A rise of the Mn and Ni EXAFS long range peaks (apparent distances in the range of 4 to 6 Å in Figure 6c,d) in **3-Ni**, that were not observed in **1-Ni** or **2-Ni**, are indicative of the formation of the extended structure like oxides and arises from multiple scattering paths. The Mn XANES and EXAFS spectra of the 3-Ni at t_{CP} = 0 h film mostly resembles the spectra of birnessites ($Mn^{III/IV}$ oxide) as shown in Figures 5e and 6e (Mg^{2+} birnessite). This implies that in the **3-Ni** film (at t_{CP} = 0 h) some fraction of Mn is reduced from the native Mn^{IV} oxidation state in **1-Ni** to Mn^{III}. A resemblance of the Mn XANES edge position to that of Mg^{2+} birnessite, which has an oxidation state of ~ 3.7, suggests that roughly 30 % of Mn is reduced to Mn^{III} and the rest remains as Mn^{IV} in the **3-Ni** film (at t_{CP} = 0 h). On the other hand, the Ni remains as Ni^{II} based on the Ni XANES edge position (Figure 5f).

Regarding the structure of **3-Ni**, Mn likely forms a layered structure that is similar to the birnessites, based on the similarities observed in both XANES and EXAFS (Figures 5e and 6e). Such structure has been observed in the Mn-oxide electrocatalysts that catalyse the oxygen evolution reaction, and a birnessite-like phase seems to be dominant when Mn is electrochemically deposited on substrates.[2d, 16a, 21b, 24] On the other hand, the Ni EXAFS

spectrum of **3-Ni** is similar to that of $Ni^{II}(OH)_2$, which has a complete cubane structure. While the peak positions of the metal-ligand (peak 1 in Figure 6e,f) and metal-metal interactions (peak 2 in Figure 6e,f) are similar to the oxides (birnessite for Mn and $Ni^{II}O$ for Ni) in both Mn and Ni EXAFS, the intensity of the peak 2 in both cases is weaker, suggesting that the metal cluster is more disordered or it has small domain sizes compared to those of bulk oxides.

A question arises whether Ni is still incorporated into the Mn birnessite-like structure in **3-Ni**. As the XPS analysis shows the retention of the Mn/Ni ratio of 3:1 in **3-Ni**, the fraction of Ni should be located either (1) systematically with Mn within the Mn layered structure, (2) randomly in the Mn layer, (3) between the Mn layers as 2^+ counter ions, or (4) Ni oxide domains are phase-separated from Mn domains.

The Mn and Ni EXAFS curve fitting of **3-Ni** (t_{CP} = 0 h) was carried out to investigate the above four possibilities (see Figure S18 in SI). The Mn EXAFS curve fitting result shows a predominant Mn-metal distance to be ~ 2.93 Å (the peak 2 region in Figure 6c,e, and also see Table S1 **3-Ni** fit #1). On the other hand, the Ni EXAFS shows a predominant Ni^{II}-metal interaction at ~2.98 Å (the peak 2 region in Figure 6d,f, and also see Table S2 **3-Ni** fit #1). This Ni^{II}–metal distance is longer than the Ni^{II}–Mn^{IV} distances (2.83 Å) in the original **1-Ni** compound, and very similar to the Ni^{II}–Ni^{II} di-μ-oxo bridged interactions (2.95 Å), typically observed in $Ni^{II}O$ oxide. While such distance could also correspond to the Ni^{II}–Mn^{III} interactions, an overall resemblance of the **3-Ni** Ni EXAFS peak positions to those of the $Ni^{II}O$ oxide spectrum indicates that the Ni domains in **3-Ni** forms a $Ni^{II}O$ oxide-like Ni–Ni interactions (see also Figure S19 for the *k* space EXAFS data).

Based on the above observations, one hypothesis is that Mn and Ni form separate domains, $Mn^{III/IV}$ with birnessite-like layered structure, and Ni with $Ni^{II}O$ oxide-like interactions (Case (4) described above). However, the fit quality of the 3rd peak region in both Mn and Ni EXAFS of **3-Ni** was not sufficient (see Figure S18 for **3-Ni**), in spite of the fact that 1st and 2nd EXAFS peaks of both Mn and Ni EXAFS fit well with the structural parameters obtained from birnessite and $Ni^{II}O$ structures, respectively. A further comparison to a series of Mn oxides suggests that the peak 3 region in the Mn EXAFS of **3-Ni** could reflect a presence of rutile-like metal-metal interactions with some oxygen with a trigonal planar coordination, that are observed in β-MnO_2 structure. To check whether such Mn–Ni interactions are present in **3-Ni** for both Mn and Ni EXAFS, an additional Mn–Ni interaction was included in the fit (Figure S18e and Tables S1 and S2, Fit 2 for **3-Ni**). The fit quality improved noticeably in the Ni EXAFS and marginally in the Mn EXAFS going from fit #1 to fit #2 in Table S1 and S2. Both Mn and Ni EXAFS suggest this metal-metal distance to be around 3.50 – 3.55 Å. Therefore, it is very likely that Mn and Ni are in a close proximity at ~ 3.5 Å in **3-Ni**. Based on the above observations together with the XPS and EDS results (Table 2) that show the Mn:Ni ratio to be close to 3:1 in **3-Ni**, a possible structural motif was built and shown in Figure 7.

In the **3-Ni** film, both Mn and Ni are sensitive to electrolysis progression as observed by the Mn and Ni XAS spectral changes during t_{CP} = 0, 1, and 5 h (Figures 5c,d and 6c,d). A reduction of the EXAFS peak intensity with no significant changes in the XANES edge

position suggests that the Mn and Ni oxide domains become highly disordered during the electrolysis.

Although the identity of the active site for hydroxide oxidation to O_2 is not known, the catalytic and spectroscopic studies reported here for $NiMn_3$ materials allow for some structure-function speculations. The method of catalyst generation leads to different behavior. Both **2-Ni** and **3-Ni** show structural changes compared to **1-Ni** based on EXAFS. The material prepared without thermal treatment, **2-Ni**, shows EXAFS features consistent with the maintenance of the $NiMn_3O_4$ moiety, though with a broader distribution of metal-metal and metal-ligand distances. The EXAFS data indicate that the major structural change occurs within the first hour of electrolysis, and that there are no significant changes between t_{CP} = 1 and 5 h. This correlates with RDV data (Figure 1c) showing a gradual lowering in overpotential, with a larger effect at early times when the material is undergoing structural changes. The material prepared by thermal treatment, **3-Ni**, has an extended oxide-like structure and is more structurally distinct from **1-Ni**. Catalytic behavior is improved for **2-Ni**. Both **2-Ni** and **3-Ni** show structural changes upon electrolysis, but they do not convert to the same material. This behavior indicates that the structural motif found in the homogeneous precursor may be roughly maintained in the heterogeneous mixed metal electrolysis catalyst, especially if high temperature treatment is avoided. The catalytic performance is affected by these structural differences.

Conclusions

Well-defined, synthetic **1-M** cubane complexes were dropcasted on ITO or glassy carbon disk electrodes and used as precursors with known 1:3 M to Mn ratio for OER electrocatalysts. Upon heat treatment at 400 °C and/or electrolysis, the OER activities of **2-M** and **3-M** were evaluated to be similar to many other reported homo- and heterometallic oxide electrocatalysts. **2-Ni** requires structural rearrangements to yield the active species. The **2-Co** film underwent composition changes to a CoO_x-like material upon prolonged electrolysis, losing the majority of Mn into the solution. The **2-Ni** film may have rearranged structurally yet still retained its Ni : Mn ratio of 1 to 3 in the final material. The distinct behaviors of the heterogeneous OER electrocatalysts described here indicate that the composition and structural changes in post-electrolysis of heterometallic catalysts is critical in understanding the behavior of these catalysts. XAS studies provided structural insights of the electrocatalysts where the resulting **2-Ni** film after electrolysis is indeed different from the initial **1-Ni** synthetic precursor, while likely maintaining the original Mn_3NiO_4 cubane-like geometry. In contrast, the thermally generated **3-Ni** develops an oxide-like extended structure, with Mn oxide birnessites with μ-oxo bridged Ni^{II}-Ni^{II} and mono-μ-oxo bridged metal-metal ($Mn^{III/IV}$-Ni^{II}) interactions. This is reminiscent of Ca-Mn oxides that display structural motifs related to the biological Oxygen Evolving Complex in Photosystem II.[2k, 25] The above structural relations suggest a catalytic function of the MMn_3O_4 cubane moiety. The use of molecular multimetallic oxido cubane precursors displaying two types of metals has been demonstrated as a facile method to access OER electrocatalysts of novel compositions and structures that allows for systematic study of changes in structure from discrete precursors to heterogeneous catalysts to post-catalysis materials.

Experimental Section

Materials synthesis and film preparation

General considerations—Unless otherwise specified, all compounds were manipulated under air. Dichloromethane (DCM) and *N,N*–dimethylformamide (DMF) were purchased from J.T. Baker and EMD Millipore respectively. High purity sodium hydroxide (NaOH) and potassium hydroxide (KOH) were purchased from Sigma Aldrich. All water used was Milli-Q water purified by a Millipore water purification system (18.2 MΩ cm resistivity). Indium tin oxide (ITO) coated glass slides (with surface resistivity 8–12 Ω /sq) were purchased from Sigma Aldrich. The complex **1-Ca** was synthesized according to literature procedure.[23a] Complexes **1-Co** and **1-Ni** are synthesized analogously to other reported **1-M**.[23b] The detailed synthesis and characterization of **1-Co** and **1-Ni** will be reported separately.

Preparation of 2-Co and 2-Ni—In a scintillation vial, 3 mg of **1-Co** or **1-Ni** was fully dissolved in DCM (0.3 mL). DMF (0.3 mL) was added into the solution, and the DCM solvent was allowed to evaporate in air. The DMF solution of **1-Co/Ni** was dropcasted using a Hamilton syringe onto 5 separate cleaned ITO coated glass substrates (with a 0.5 cm × 0.5 cm window or geometric surface area of 0.25 cm^2) or glassy carbon (GC) disks equally in 60 μL portions. The dropcasted solution on the electrodes was then dried under vacuum over 1 h to yield a thick film on the ITO. These resulting films, **2-Co** and **2-Ni**, were used as precursors to the catalytically species after electrolysis.

Preparation of 3-Co and 3-Ni—The dried films, **2-Co** and **2-Ni**, on ITO coated glass substrate were then heated at 400 °C in the thermolyne muffle furnace for ≥ 4 h to remove the organic ligands and generate non-uniform, thin metal oxide film on the ITO. Removal of organic ligands from **1-Co** was confirmed by thermogravimetric analysis (TGA) (Figure S1), and the analogous event is assumed to occur for **1-Ni**. These resulting films, **3-Co** and **3-Ni**, are used as is for further electrochemical experiments.

Note: preparation of **3-Co**/**Ni** on the GC disks was not conducted due to the possibility of compromising the GC electrode quality under high heat (400 °C) for prolonged period of time.

Electrochemistry

Electrochemical measurements of **1-Co** and **1-Ni** were conducted with a Solarton 1287/1260 potentiostat/ galvanostat with a built-in electrochemical impedance spectroscopy (EIS) analyzer. The working electrode was ITO on glass substrate, and catalysts were deposited as described above. The auxiliary electrode was a Pt mesh electrode, and the reference electrode was a BASi or CH Instruments Ag/AgCl reference electrode. All potentials reported in this manuscript were converted to NHE reference scale.

Cyclic voltammetry—Electrocatalyst films with geometric surface area of 0.25 cm^2 on ITO was used as the working electrode with Pt mesh as the auxiliary electrode and Ag/AgCl reference electrode. A 2-compartment cell was used for cyclic voltammetry experiments

filled with 0.1 M KOH (pH 13) solution. Cyclic voltammograms were collected at 100 mV/s.

Tafel plots—Current-potential data were obtained by performing chronoamperometry in 0.1 M KOH electrolyte at a variety of applied potentials in a two-compartment cell. The geometric surface area of the catalyst was 0.25 cm^2 prepared as mentioned above for **2-M** and **3-M**. Steady-state currents were measured at a variety of applied potentials while the solution was stirred, starting at 1.75 V and proceeding in 10 mV steps to 1.5 V vs. RHE. The current reached a steady state at a certain potential within 1–2 minutes. The measurements were made three times and averaged with the variation in steady-state current <5%.

Rotating disk voltammetry (RDV)—All activity, stability, and electrochemically-active surface area (ECSA) measurements on the glassy carbon (GC) disk electrodes were conducted with a Bio-Logic VMP3 multichannel potentiostat/galvanostat with a built-in EIS analyzer. The working electrodes were 5 mm diameter disk electrodes, and catalysts were deposited as described above. The working electrodes were mounted in a Pine Instrument Company E6-series ChangeDisk rotating disk electrode assembly in an MSR rotator. The auxiliary electrodes were carbon rods (99.999%, Alfa Aesar), and the reference electrode was a commercial saturated calomel electrode (SCE) (CH-Instruments) that was externally referenced to a solution of ferrocene monocarboxylic acid (Sigma-Aldrich) in a 0.2 M phosphate buffer at pH 7 (0.284 V vs SCE).[28] Data were recorded using the Bio- Logic EC-Lab and EC-Lab Express software packages. Electrochemical experiments were carried out according to a previously described protocol for the evaluation of heterogeneous electrocatalysts for the OER[9i] to compare the OER performance of **2-Co** and **2-Ni** against selected electrodeposited electrocatalysts under identical conditions.

Electrochemically-active surface area, ECSA, of each catalyst was determined by estimating the double-layer capacitance, C_{DL}, of the system from cyclic voltammograms as previously described.[9i, 9k, 26] Briefly, a non-Faradaic region was established for each system from CV. All current in this region is assumed to be due to double-layer charging, and, thus, the measured charging current, i_c, is equal to the product of the scan rate, ν, and the double-layer capacitance (Eq 2).[26–27]

$$i_c = \nu C_{DL} \quad \text{(Eq. 2)}$$

The electrochemical surface area is determined by dividing the estimated C_{DL}, of each system by the specific capacitance of the sample. For the purpose of this study, we use a specific capacitance of 0.040 mF cm^{-2} which is a typical value for a metal electrode in aqueous NaOH solutions.[9i] The ECSA values determined from these measurements are order-of-magnitude approximations for rough comparison of electroactive surface areas.[9i, 9k]

Oxygen evolution faradaic efficiency measurements—The experiment was performed in a custom built two-compartment gas-tight electrochemical cell with a 14/20 port on each compartment and a Schlenk connection with a Teflon valve on the working compartment. The cell volume was 154 mL. A NeoFox oxygen sensing system by Ocean

Optics with FOXY fluorescence probe was used in O_2 detection. The oxygen concentration was monitored throughout the measurement, and was tabulated via measured values from a fluorescence detector. These values were calibrated using the standard concentration of oxygen in air as 20.9% partial pressure of O_2 atmosphere. The cell was initially evacuated under vacuum. 54 mL of degassed 0.1 M KOH electrolyte solution was canula transferred into the cell under positive N_2 pressure, and the headspace used as a 0.0% O_2 atmosphere. The calculated volume of the headspace was 96 mL. An Ag/AgCl electrode was the reference electrode and placed in one compartment, while the counter electrode was a Pt mesh positioned in a separate, fritted compartment.

All catalysts used were prepared by subjecting the film through chronopotentiometry experiments for 5 h prior to oxygen evolution measurements. The ITO electrode with the catalyst film was clipped inside the electrochemical cell prior to evacuating the cell under vacuum mentioned above.

To ensure no leakage occurred, the partial pressure of O_2 was measured for 2 h in the absence of an applied potential. Chronopotentiometry experiment was run at a steady current of 1 mA cm^{-2} for 2–4 h with stirring of the solution. Upon termination of electrolysis, the O_2 signal was recorded for an additional 2 h. At the conclusion of the experiment, the volume of the solution and the volume of the headspace in the working compartment were measured again (54 mL and 96 mL, respectively). The blue curve in Figure S4 was calculated by dividing the charge passed in the electrolysis by 4F (theoretical yield) and the red curve was calculated by converting the measured partial pressure of O_2 into μmols, correcting for the O_2 in solution using Henry's Law (experimental yield).

Structural characterization

Powder X-Ray diffraction (XRD)—Powder XRD patterns were obtained with a PANalytical X'Pert Pro rotating anode X-ray diffractometer (185 mm) using Cu Kα radiation (λ = 1.5405 Å). Data was collected at a scan rate of 1°/min. A pattern was collected for an ITO-coated glass substrate and for the electrocatalysts prepared (Fig. S1). The ITO peaks were observed as the only signals arising from all XRD pattern of the electrocatalysts. Given that the final deposited catalyst sample is ~100 nm thick, the presence of peaks from the relatively thin ITO layer and the absence of any non-ITO associated peaks indicate that the catalyst material is probably too thin or amorphous.

Scanning electron microscopy (SEM)—Scanning-electron micrograph (SEM) was obtained using a high-resolution analytical scanning electron microscope (ZEISS 1550VP) at an accelerating voltage of 10 kV with a working distance of 8 mm and an inlens secondary electron detector.

X-ray Absorption Spectroscopy (XAS)—X-ray absorption spectra of the electrode samples were collected at the Stanford Synchrotron Radiation Lightsource (SSRL) on beamline 7–3 at an electron energy of 3.0 GeV with an average current of 500 mA. The incoming X-ray was monochromatized by a Si(220) double-crystal monochromator. The intensity of the incident X-ray was monitored by an N_2-filled ion chamber (I_0) in front of the sample. Data were collected as fluorescence excitation spectra with a Ge 30 element detector

(Canberra). The monochromator energy was calibrated by the pre-edge peak top of $KMnO_4$ standard at 6543.30 eV for Mn XAS, and the rising edge position of Ni foil at 8333.0 eV for Ni XAS. The standard was placed between two N_2-filled ionization chambers (I_1 and I_2) after the sample. All data were collected *ex situ* at room temperature before or after electrochemistry.

Data reduction of the extended X-ray absorption fine structure (EXAFS) spectra was performed using SixPack (Dr. Samuel Webb, SSRL). Pre-edge and post-edge backgrounds were subtracted from the XAS spectra, and the results were normalized with respect to edge height. Background removal in *k*-space was achieved through a five-domain cubic spline. Curve fitting was performed with Artemis and IFEFFIT software using *ab initio*-calculated phases and amplitudes from the program FEFF 8.2.[29] These *ab initio* phases and amplitudes were used in the EXAFS equation:

$$\chi(k)=S_0^2\sum_j \frac{N_j}{kR_j^2} f_{\mathrm{eff}_j}(\pi,k,R_j)e^{-2\sigma_j^2k^2}e^{-2R_j/\lambda_j(k)}\ \sin(2kR_j+\phi_{ij}(k)) \quad \text{(equation 2)}$$

The neighboring atoms to the central atom(s) are divided into *j* shells, with all atoms with the same atomic number and distance from the central atom grouped into a single shell. Within each shell, the coordination number N_j denotes the number of neighboring atoms in shell *j* at a distance of R_j from the central atom. The $f_{eff_j}(\pi, k, R_j)$ term is the *ab initio* amplitude function for shell *j*, and the Debye-Waller term $e^{-2\sigma_j^2k^2}$ accounts for damping due to static and thermal disorder in absorber-backscatterer distances. The mean free path term $e^{-2R_j/\lambda_j(k)}$ reflects losses due to inelastic scattering, where $\lambda_j(k)$ is the electron mean free path. The oscillations in the EXAFS spectrum are reflected in the sinusoidal term, $\sin(2kR_j + \varphi_{ij}(k))$ where $\varphi_{ij}(k)$ is the *ab initio* phase function for shell *j*. S_0^2 is an amplitude reduction factor due to shake-up/shake-off processes at the central atom(s). The EXAFS equation was used to fit the experimental data using *N*, *R*, and the EXAFS Debye-Waller factor (σ^2) as variable parameters. E_0 was defined as 6561.3 eV and the S_0^2 value was fixed to 0.70 for the energy (eV) to wave vector (*k*, $Å^{-1}$) axis conversion for Mn XAS, and the E_0 of 8340 eV and the S_0^2 of 0.95 were used for Ni XAS.

Elemental composition analyses

X-ray photoelectron spectroscopy (XPS)—X-ray photoelectron spectroscopy (XPS) data were collected using a Surface Science Instruments M-Probe ESCA controlled by Hawk Data Collection software (Service Physics, Bend OR; V7.04.04). The monochromatic X-ray source was the Al K α line at 1486.6 eV, directed at 35° to the sample surface (55° off normal). Emitted photoelectrons were collected at an angle of 35° with respect to the sample surface (55° off normal) by a hemispherical analyzer. The angle between the electron collection lens and X-ray source is 71°. Low-resolution survey spectra were acquired between binding energies of 1–1100 eV. Higher-resolution detailed scans, with a resolution of ~0.8 eV, were collected on individual XPS lines of interest. The sample chamber was maintained at $< 2 \times 10^{-9}$ Torr. Analysis of the spectra was done using the Hawk Data Analysis software (V7.04.04) and the CasaXPS Version 2.3.15 software package.

Energy dispersive X-ray spectroscopy (EDS) and elemental mapping—An Oxford X-Max SDD energy-dispersive X-ray spectrometer (EDS) equipped in the SEM instrument was used at a working distance of 12 mm using an accelerating voltage of 20 kV.

Inductively coupled–mass spectrometry (ICP–MS)—Inductively coupled plasma mass spectrometry (ICP-MS) data were collected using a Hewlett-Packard 4500 ICP-MS System with a Babbington nebulizer and a Scott-type spray chamber maintained at 5 °C. The plasma was operated at 1250 W. All samples were diluted to concentrations between 10–20 ppb and analyzed against a standard curve of known concentrations of specific metals.

Acknowledgments

This work was supported by Caltech, the NSF CAREER CHE-1151918 and the NIH R01 GM102687A (T.A.). T.A. is a Sloan, Cottrell, and Dreyfus fellow. Rotating-disk voltammetry and 2-h stability measurements are based on work performed by the Joint Center for Artificial Photosynthesis, a DOE Energy Innovation Hub, supported through the Office of Science of the U.S. Department of Energy under Award No. DE-SC0004993. Portions of this research were carried out at the SSRL, operated by Stanford University for the U.S. DOE Office of Science, and supported by the DOE and NIH. X-ray spectroscopy studies were supported by the NIH (R.T.) and by the Director of the OBES, Division of Chemical Sciences, Geosciences, and Biosciences, DOE (J.Y.). We thank James D. Blakemore for helpful discussions, Nathan Dalleska for assistance in ICP-MS data acquisition, and Tim Davenport for assistance in TGA studies. We thank Drs. Jordi Cabana and Ulrike Boesenberg for providing us the NiO reference spectrum. Research was in part carried out at the Molecular Materials Research Center of the Beckman Institute of the California Institute of Technology. This project benefited from the use of instrumentation made available by the Caltech Environmental Analysis Center.

References

1. a) Cook TR, Dogutan DK, Reece SY, Surendranath Y, Teets TS, Nocera DG. Chem. Rev. 2010; 110:6474–6502. [PubMed: 21062098] b) Walter MG, Warren EL, McKone JR, Boettcher SW, Mi QX, Santori EA, Lewis NS. Chem. Rev. 2010; 110:6446–6473. [PubMed: 21062097] c) Trasatti, S. Interfacial Electrochemistry: Theory, Practice, Applications. New York: Marcel Dekker; 1999.
2. a) Kanan MW, Nocera DG. Science. 2008; 321:1072–1075. [PubMed: 18669820] b) Gorlin Y, Jaramillo TF. J. Am. Chem. Soc. 2010; 132:13612–13614. [PubMed: 20839797] c) Dinca M, Surendranath Y, Nocera DG. Proc. Natl. Acad. Sci. USA. 2010; 107:10337–10341. [PubMed: 20457931] d) Zaharieva I, Chernev P, Risch M, Klingan K, Kohlhoff M, Fischer A, Dau H. Energy Environ. Sci. 2012; 5:7081–7089.e) Schley ND, Blakemore JD, Subbaiyan NK, Incarvito CD, D'Souza F, Crabtree RH, Brudvig GW. J. Am. Chem. Soc. 2011; 133:10473–10481. [PubMed: 21671679] f) Suntivich J, May KJ, Gasteiger HA, Goodenough JB, Shao-Horn Y. Science. 2011; 334:1383–1385. [PubMed: 22033519] g) Subbaraman R, Tripkovic D, Chang KC, Strmcnik D, Paulikas AP, Hirunsit P, Chan M, Greeley J, Stamenkovic V, Markovic NM. Nature Mater. 2012; 11:550–557. [PubMed: 22561903] h) Jiao F, Frei H. Energy Environ. Sci. 2010; 3:1018–1027.i) Yang JH, Walczak K, Anzenberg E, Toma FM, Yuan GB, Beeman J, Schwartzberg A, Lin YJ, Hettick M, Javey A, Ager JW, Yano J, Frei H, Sharp ID. J. Am. Chem. Soc. 2014; 136:6191–6194. [PubMed: 24720554] j) Rumberger EMW, Ahn HS, Bell AT, Tilley TD. Dalton Trans. 2013; 42:12238–12247. [PubMed: 23861177] k) Zaharieva I, Najafpour MM, Wiechen M, Haumann M, Kurz P, Dau H. Energy Environ. Sci. 2011; 4:2400–2408.
3. a) Rossmeisl J, Logadottir A, Norskov JK. Chem. Phys. 2005; 319:178–184.b) Conway, BE.; Tilak, BV. Advances in Catalysis. Vol. 38. New York: Academic Press; 1992.
4. a) Bockris JO, Otagawa T. J. Phys. Chem. 1983; 87:2960–2971.b) Bockris JO, Otagawa T. J. Electrochem. Soc. 1984; 131:290–302.
5. Rasiyah P, Tseung ACC. J. Electrochem. Soc. 1984; 131:803–808.
6. Trasatti S. J. Electroanal. Chem. 1980; 111:125–131.
7. a) Matsumoto Y, Sato E. Mater. Chem. Phys. 1986; 14:397–426.b) Hoare, JP. Encyclopedia of Electrochemistry of the Elements. Vol. 2. New York: Marcel Dekker; 1982.
8. Trasatti S. Electrochim. Acta. 1984; 29:1503–1512.

9. a) Corrigan DA. J. Electrochem. Soc. 1987; 134:377–384.b) Corrigan DA, Bendert RM. J. Electrochem. Soc. 1989; 136:723–728.c) Merrill MD, Dougherty RC. J. Phys. Chem. C. 2008; 112:3655–3666.d) Trotochaud L, Young SL, Ranney JK, Boettcher SW. J. Am. Chem. Soc. 2014; 136:6744–6753. [PubMed: 24779732] e) Landon J, Demeter E, Inoglu N, Keturakis C, Wachs IE, Vasic R, Frenkel AI, Kitchin JR. ACS Catal. 2012; 2:1793–1801.f) Gong M, Li YG, Wang HL, Liang YY, Wu JZ, Zhou JG, Wang J, Regier T, Wei F, Dai HJ. J. Am. Chem. Soc. 2013; 135:8452–8455. [PubMed: 23701670] g) Louie MW, Bell AT. J. Am. Chem. Soc. 2013; 135:12329–12337. [PubMed: 23859025] h) Trotochaud L, Ranney JK, Williams KN, Boettcher SW. J. Am. Chem. Soc. 2012; 134:17253–17261. [PubMed: 22991896] i) McCrory CCL, Jung SH, Peters JC, Jaramillo TF. J. Am. Chem. Soc. 2013; 135:16977–16987. [PubMed: 24171402] j) Smith AM, Trotochaud L, Burke MS, Boettcher SW. Chem. Commun. 2015k) McCrory CCL, Jung S, Ferrer IM, Chatman SM, Peters JC, Jaramillo TF. J. Am. Chem. Soc. 2015; 137:4347–4357. [PubMed: 25668483]
10. a) Jasem SM, Tseung ACC. J. Electrochem. Soc. 1979; 126:1353–1360.b) Ho JCK, Piron DL. J. Appl. Electrochem. 1996; 26:515–521.
11. a) Kibria AKMF, Tarafdar SA. Int. J. Hydrogen Energ. 2002; 27:879–884.b) Li XH, Walsh FC, Pletcher D. Phys. Chem. Chem. Phys. 2011; 13:1162–1167. [PubMed: 21076764]
12. Burke MS, Kast MG, Trotochaud L, Smith AM, Boettcher SW. J. Am. Chem. Soc. 2015
13. Singh RN, Madhua, Awasthi R, Sinha ASK. Electrochim. Acta. 2009; 54:3020–3025.
14. Singh RN, Madhu, Awasthi R, Tiwari SK. Int. J. Hydrogen Energ. 2009; 34:4693–4700.
15. Singh RN, Pandey JP, Singh NK, Lal B, Chartier P, Koenig JF. Electrochim. Acta. 2000; 45:1911–1919.
16. a) Wiechen M, Zaharieva I, Dau H, Kurz P. Chem. Sci. 2012; 3:2330–2339.b) Kim J, Yin X, Tsao KC, Fang SH, Yang H. J. Am. Chem. Soc. 2014; 136:14646–14649. [PubMed: 25295698]
17. Singh RN, Singh NK, Singh JP. Electrochim. Acta. 2002; 47:3873–3879.
18. a) Chen JYC, Miller JT, Gerken JB, Stahl SS. Energy Environ. Sci. 2014; 7:1382–1386.b) Gerken JB, Shaner SE, Masse RC, Porubsky NJ, Stahl SS. Energy Environ. Sci. 2014; 7:2376–2382.c) Gerken JB, Chen JYC, Masse RC, Powell AB, Stahl SS. Angew. Chem. Int. Edit. 2012; 51:6676–6680.d) Haber JA, Cai Y, Jung SH, Xiang CX, Mitrovic S, Jin J, Bell AT, Gregoire JM. Energy Environ. Sci. 2014; 7:682–688.
19. a) Haber JA, Xiang CX, Guevarra D, Jung SH, Jin J, Gregoire JM. Chemelectrochem. 2014; 1:524–528.b) Cattarin S, Frateur I, Guerriero P, Musiani M. Electrochim. Acta. 2000; 45:2279–2288.
20. a) Smith RDL, Prevot MS, Fagan RD, Zhang ZP, Sedach PA, Siu MKJ, Trudel S, Berlinguette CP. Science. 2013; 340:60–63. [PubMed: 23539180] b) Smith RDL, Prevot MS, Fagan RD, Trudel S, Berlinguette CP. J. Am. Chem. Soc. 2013; 135:11580–11596. [PubMed: 23883103] c) Zhang CJ, Trudel S, Berlinguette CP. Eur. J. Inorg. Chem. 2014:660–664.
21. a) Gorlin Y, Chung CJ, Benck JD, Nordlund D, Seitz L, Weng TC, Sokaras D, Clemens BM, Jaramillo TF. J. Am. Chem. Soc. 2014; 136:4920–4926. [PubMed: 24661269] b) Gorlin Y, Lassalle-Kaiser B, Benck JD, Gul S, Webb SM, Yachandra VK, Yano J, Jaramillo TF. J. Am. Chem. Soc. 2013; 135:8525–8534. [PubMed: 23758050]
22. a) Karkas MD, Verho O, Johnston EV, Akermark B. Chem. Rev. 2014; 114:11863–12001. [PubMed: 25354019] b) Ullman AM, Liu Y, Huynh M, Bediako DK, Wang HS, Anderson BL, Powers DC, Breen JJ, Abruna HD, Nocera DG. J. Am. Chem. Soc. 2014; 136:17681–17688. [PubMed: 25407218] c) Najafpour MM, Moghaddam AN, Dau H, Zaharieva I. J. Am. Chem. Soc. 2014; 136:7245–7248. [PubMed: 24798550] d) Wiechen M, Berends HM, Kurz P. Dalton Trans. 2012; 41:21–31. [PubMed: 22068958] e) Hocking RK, Brimblecombe R, Chang LY, Singh A, Cheah MH, Glover C, Casey WH, Spiccia L. Nature Chem. 2011; 3:461–466. [PubMed: 21602861] f) Brimblecombe R, Swiegers GF, Dismukes GC, Spiccia L. Angew. Chem. Int. Edit. 2008; 47:7335–7338.g) Stracke JJ, Finke RG. J. Am. Chem. Soc. 2011; 133:14872–14875. [PubMed: 21894961] h) Yagi M, Narita K. J. Am. Chem. Soc. 2004; 126:8084–8085. [PubMed: 15225027] i) Lai YH, King TC, Wright DS, Reisner E. Chem. Eur. J. 2013; 19:12943–12947. [PubMed: 23946244] j) Lai YH, Lin CY, Lv YK, King TC, Steiner A, Muresan NM, Gan LH, Wright DS, Reisner E. Chem. Commun. 2013; 49:4331–4333.
23. a) Kanady JS, Tsui EY, Day MW, Agapie T. Science. 2011; 333:733–736. [PubMed: 21817047] b) Tsui EY, Agapie T. Proc. Natl. Acad. Sci. USA. 2013; 110:10084–10088. [PubMed: 23744039]

24. a) Bediako DK, Lassalle-Kaiser B, Surendranath Y, Yano J, Yachandra VK, Nocera DG. J. Am. Chem. Soc. 2012; 134:6801–6809. [PubMed: 22417283] b) Kanan MW, Yano J, Surendranath Y, Dinca M, Yachandra VK, Nocera DG. J. Am. Chem. Soc. 2010; 132:13692–13701. [PubMed: 20839862]
25. a) Umena Y, Kawakami K, Shen JR, Kamiya N. Nature. 2011; 473:55-U65. [PubMed: 21499260] b) Ferreira KN, Iverson TM, Maghlaoui K, Barber J, Iwata S. Science. 2004; 303:1831–1838. [PubMed: 14764885]
26. Benck JD, Chen ZB, Kuritzky LY, Forman AJ, Jaramillo TF. ACS Catal. 2012; 2:1916–1923.
27. a) Trasatti S, Petrii OA. Pure Appl. Chem. 1991; 63:711–734.b) Bockris JO, Srinivas S. J. Electroanal. Chem. 1966; 11:350-&.c) Boggio R, Carugati A, Trasatti S. J. Appl. Electrochem. 1987; 17:828–840.
28. Liaudet E, Battaglini F, Calvo EJ. J. Electroanal. Chem. 1990; 293:55–68.
29. a) Newville M. J. Synchotr. Rad. 2001; 8:322–324.b) Rehr JJ, Albers RC. Rev. Modern. Phys. 2000; 72:621–654.

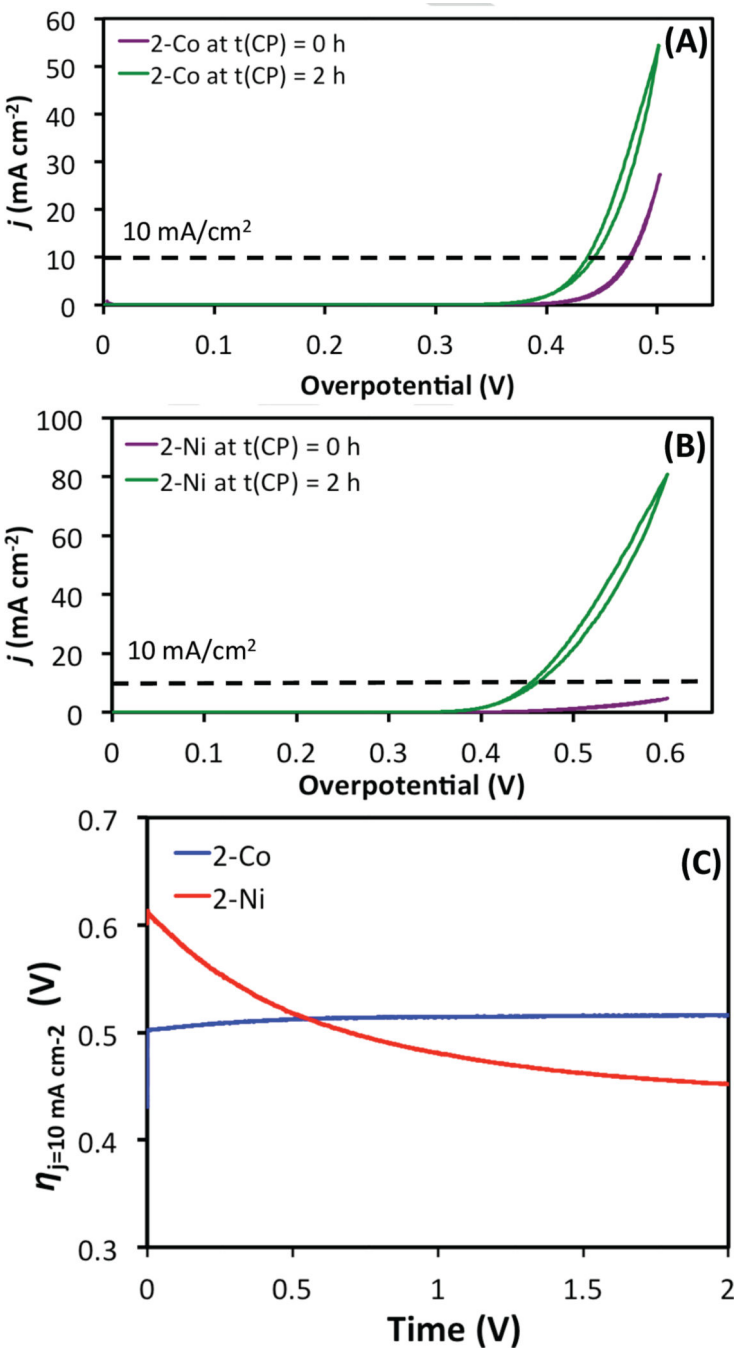

Figure 1.

RDV of **2-Co** (A) and **2-Ni** (B) on glassy carbon disks before and after 2 h CP in 1 M NaOH solution; (C) stability test of 2 over 2 h of CP held at 10 mA cm^{-2} at 1600 rpm rotation rate.

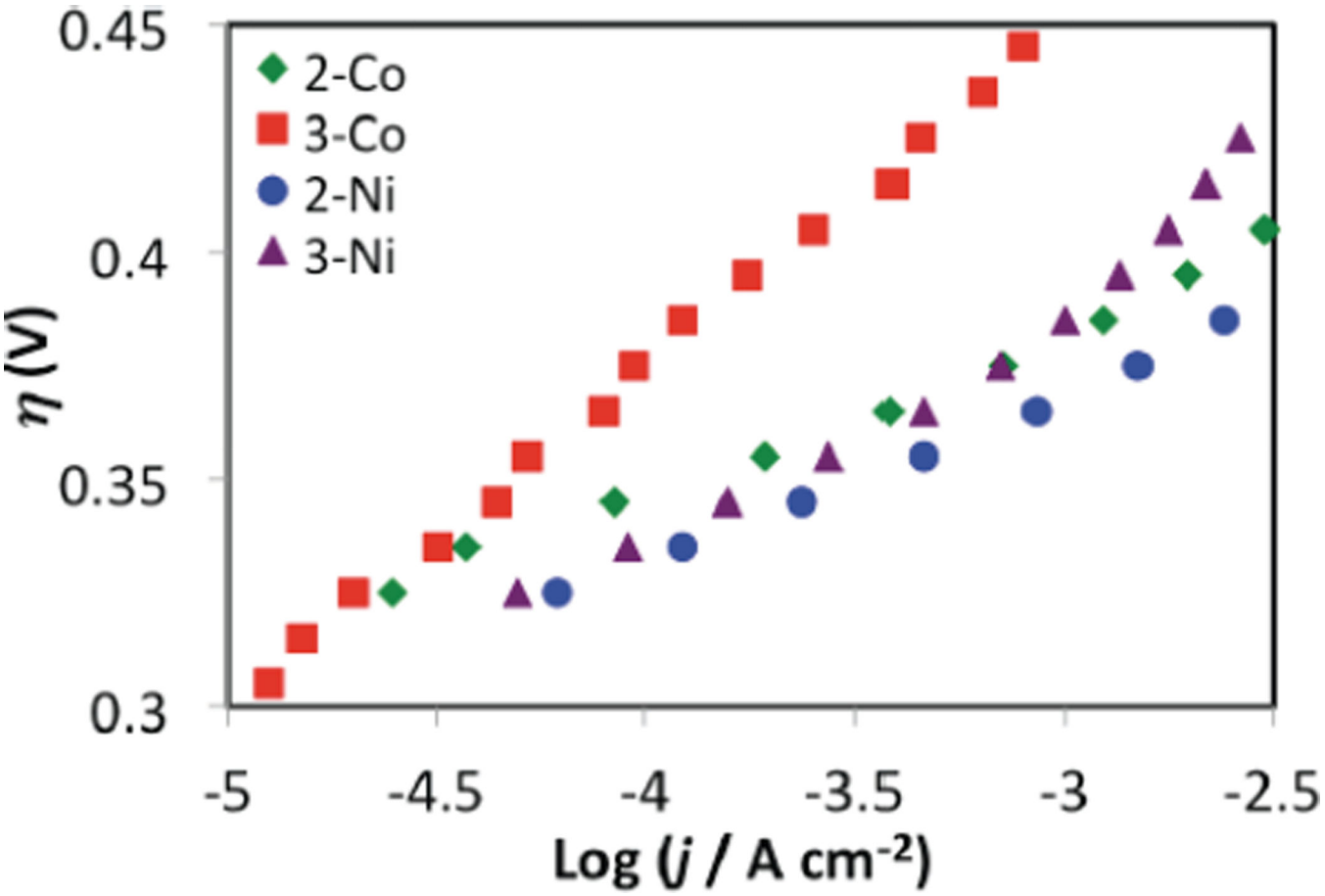

Figure 2.
Tafel plots of the metal oxides on ITO: **2-Co** (green diamond), **3-Co** (red squares), 2-Ni (blue circles), and 3-Ni (purple triangles).

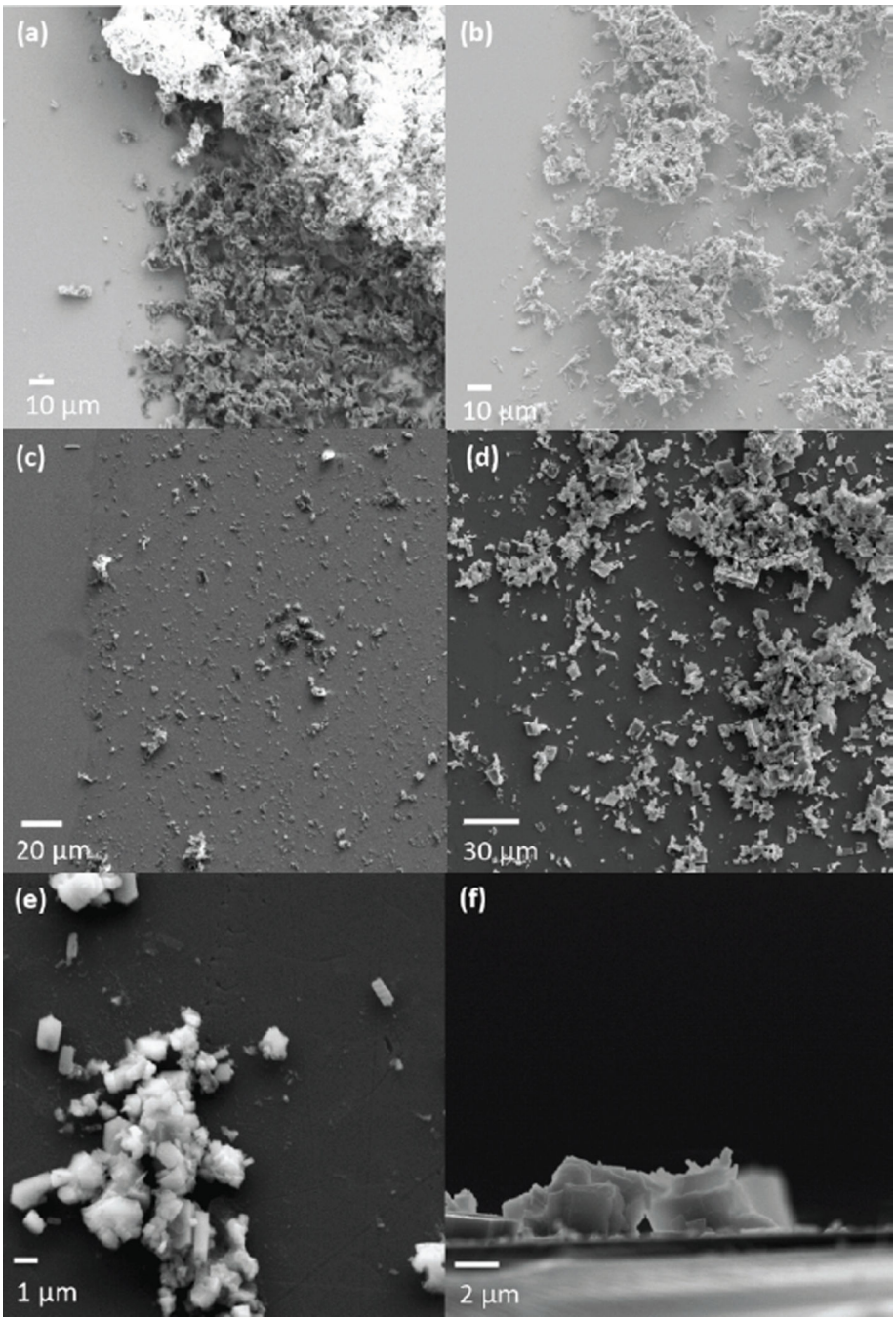

Figure 3.

SEM images of ITO electrode surfaces with: (a) **1-Co** initially dropcasted pre-electrolysis; (b) **3-Co** pre- and post-electrolysis; (c) **2-Co** post-electrolysis; (d) **3-Ni** pre- and post-electrolysis; (e) **2-Ni** post-electrolysis; (f) cross section side-view of electrode with **2-Ni** post-electrolysis

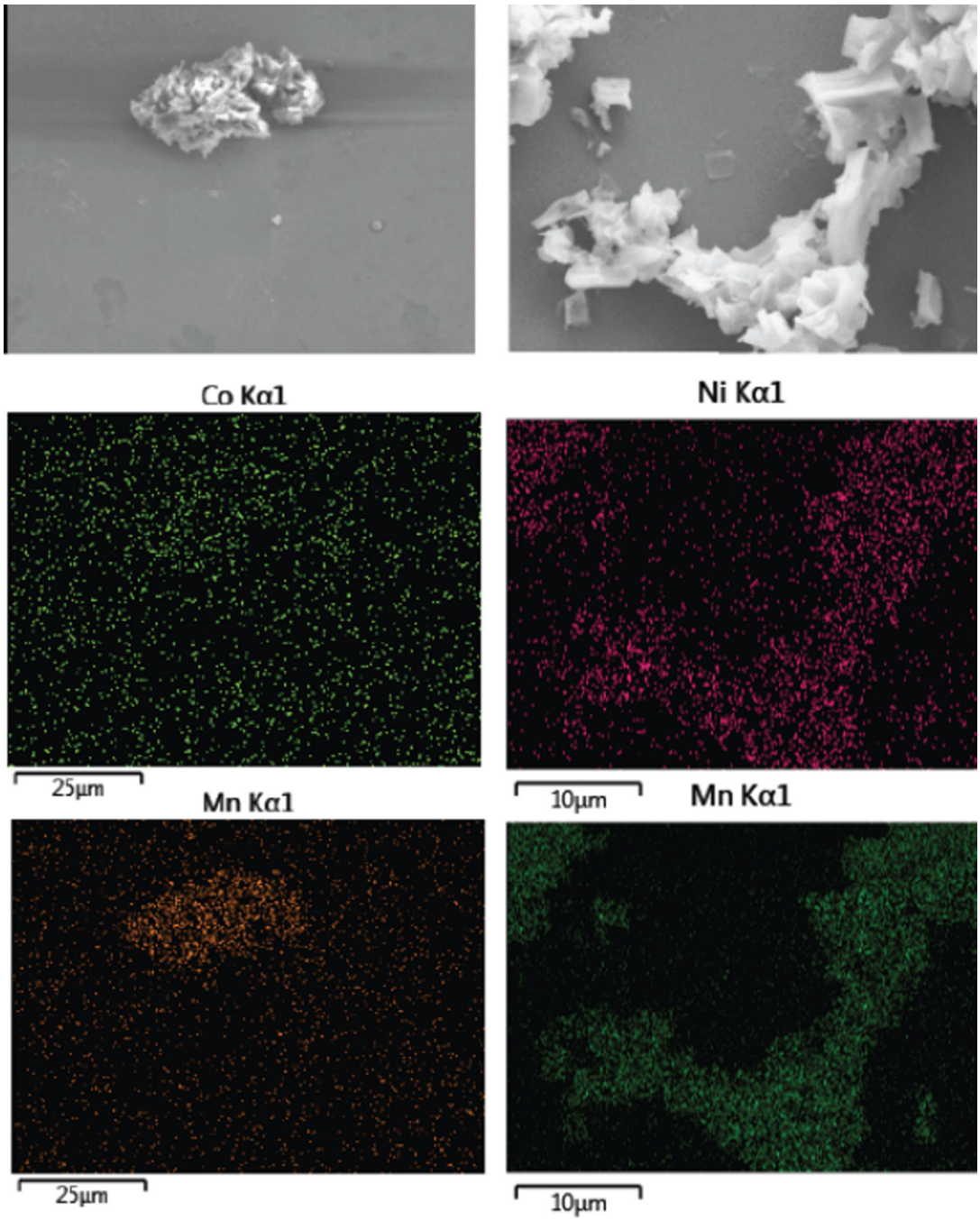

Figure 4.

SEM images and elemental mappings of **2-Co** (left) and **3-Ni** (right) on ITO after electrolysis, displaying the SEM image with the corresponding Mn and Co/Ni Kα1 compositional maps.

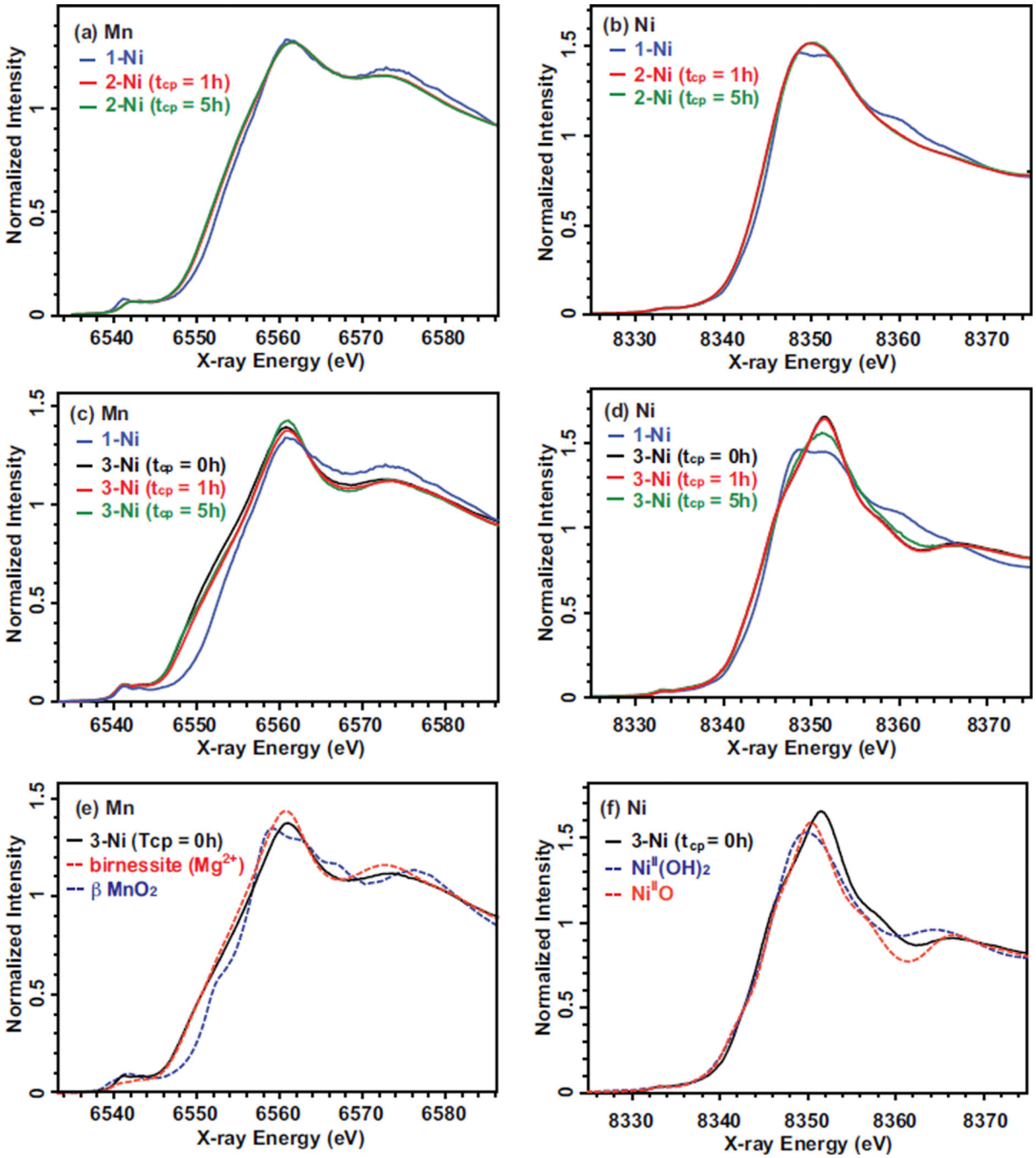

Figure 5.

Mn (left) and Ni (right) XANES spectra of **1-Ni** with **2-Ni** at t_{CP} = 1 and 5 h (a,b), and **3-Ni** (c,d) films at t_{CP} = 0, 1, 5 h. The spectra of **3-Ni** at t_{CP} = 0 h were also compared with those of Mn and Ni oxides (e,f).

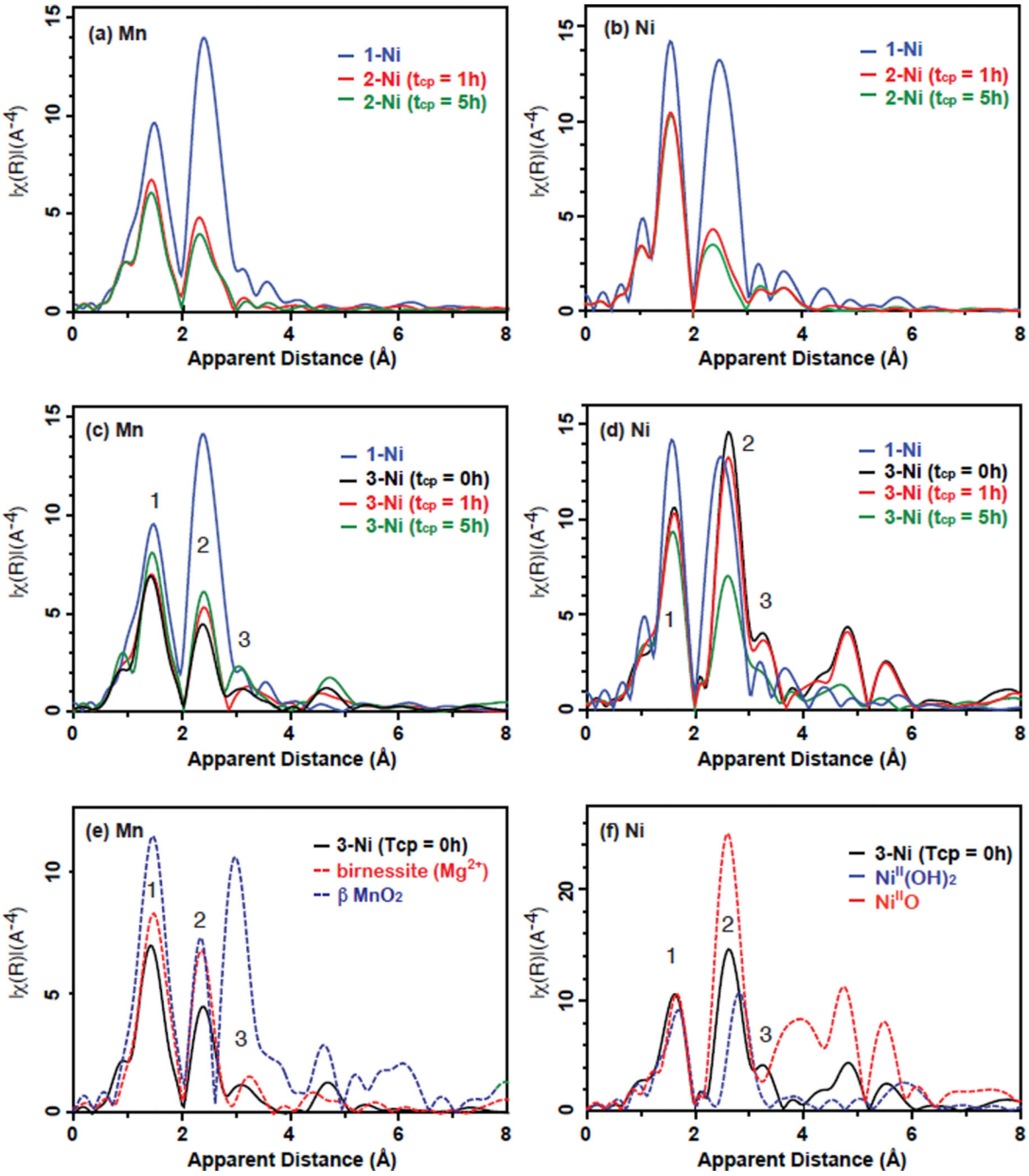

Figure 6.

Mn (left) and Ni (right) EXAFS spectra of **1-Ni** with **2-Ni** at t_{CP} = 1 and 5 h (a,b), and **3-Ni** (c,d) films at t_{CP} = 0, 1, 5 h. The spectra of **3-Ni** at t_{CP} = 0 h were also compared with those of Mn and Ni oxides (e,f).

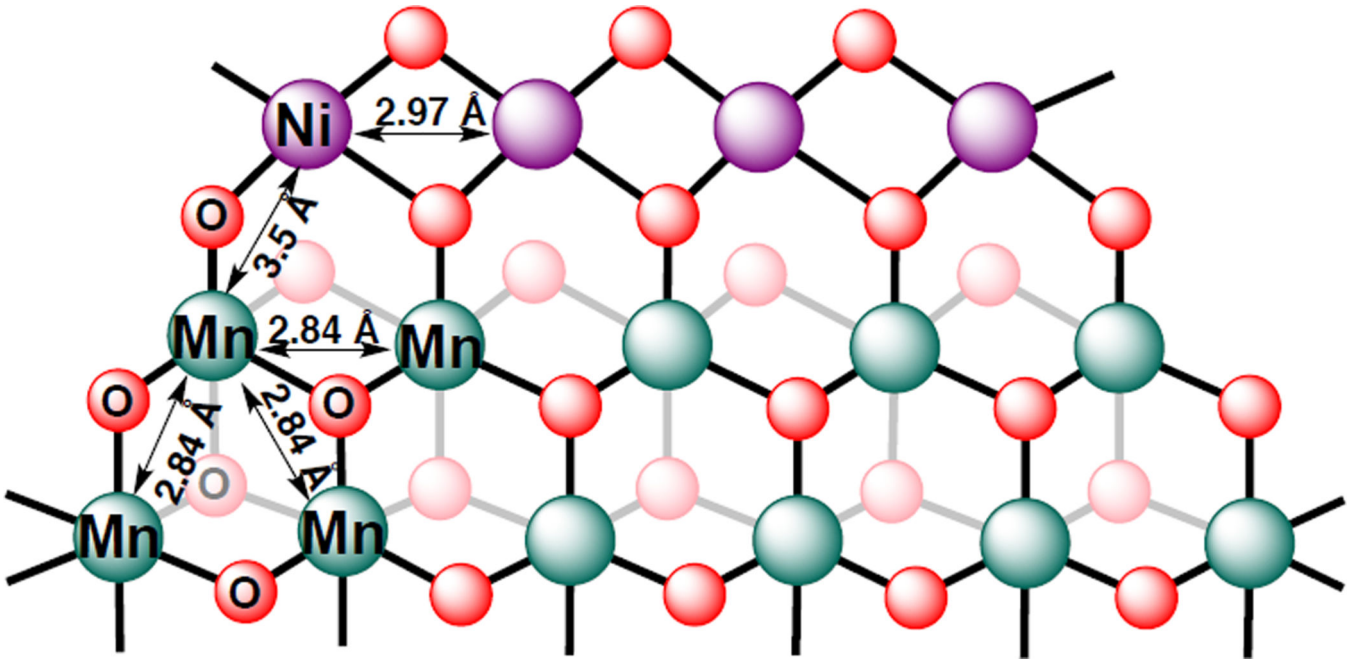

Figure 7.

Structural model for **3-Ni**. Bridging oxo/hydroxo ligands are shown in red, Mn centers are shown in green, and Ni centers are shown in purple. Estimated metal–metal and metal–ligand distances based on the EXAFS data are shown.

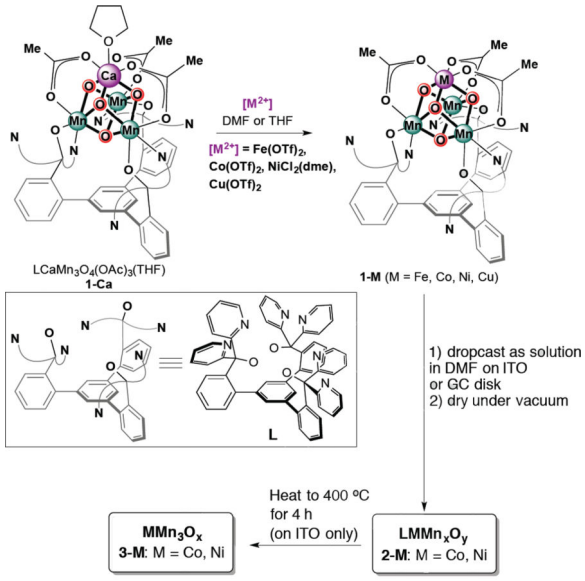

Scheme 1.

Synthetic route for the preparation of $LMMn_xO_y$ (**2**) and MMn_3O_x (**3**). Heating of **2** at 400 °C yields **3** where all the organic ligand was calcined.

Table 1

Tafel slopes and overpotential parameters for **2** and **3**

Catalyst	Tafel slope (mV dec^{-1}) *[a]*	$\eta_{j=1mA\ cm-2}$ (V)*[a]*	$\eta_{j=10mA\ cm-2}$ (V) *[b]*
2-Co	42 ± 5	0.39 ± 0.02	0.47 ± 0.01
3-Co	69 ± 9	0.45 ± 0.2	–
2-Ni	40 ± 4	0.37 ± 0.01	0.42 ± 0.01
3-Ni	58 ± 1	0.38 ± 0.01	–

*[a]*Tafel slope and $\eta_{j=1\ mA\ cm-2}$ parameters are derived from CP experiments on materials **2-M** and **3-M** dropcasted on ITO glass. Electrochemical experiments were performed in 0.1 M KOH

*[b]***2-Co** and **2-Ni** were dropcasted on GC disk for various electrochemical experiments using RDV[9i]

Table 2

Normalized relative metal stoichiometry of catalyst films by XPS, EDS, and ICP-MS

	XPS						EDS			ICP-MS		
	Before electrolysis			*After electrolysis*			*After electrolysis*					
Catalyst	**Co**	**Ni**	**Mn**	**Co**	**Ni**	**Mn**	**Co**	**Ni**	**Mn**	**Co**	**Ni**	**Mn**
2-Co	1	-	3.4 ± 0.2	1	-	1.2 ± 0.3	1	-	1.3 ± 0.7	1	-	1.1 ± 0.2
3-Co	1	-	3.9 ± 0.4	1	-	3.9 ± 1.0	1	-	3.1 ± 0.4	n/a		
2-Ni	-	1	2.8 ± 0.1	-	1	3.4 ± 0.3	-	1	2.9 ± 0.8	-	1	2.1 ± 0.3
3-Ni	-	1	3.4 ± 0.2	-	1	3.6 ± 1.1	-	1	2.8 ± 0.3	n/a		

[a] ICP–MS analyses were only performed on **2–Co** and **2–Ni** after electrolysis on GC disks to prevent signal saturation from ITO

Table 3

Comparison of **2-Co** and **2-Ni** to selected metal oxide OER electrocatalysts

Catalyst	ECSA/cm^2	$\eta_{t=2h}$/V	ε
Co-(b)[a]	1.9 ± 0.6	0.40 ± 0.04	0.97 ± 0.01
Co/P-(a)[a] (“CoP_i”)	3.3 ± 1.8	0.38 ± 0.02	0.91 ± 0.05
Ru-(a)[a]	14 ± 4	0.32 ± 0.02	0.93 ± 0.07
Ni-(b)[a]	0.4 ± 0.2	0.47 ± 0.03	0.90 ± 0.02
NiCo-(c)[a]	1.8 ± 0.8	0.35 ± 0.01	0.92 ± 0.02
NiFe-(b)[a]	0.8 ± 0.2	0.37 ± 0.02	0.93 ± 0.02
NiMoFe-(b)[a]	1.8 ± 0.6	0.33 ± 0.02	0.97 ± 0.05
GC background[b]	1.9 ± 0.9	1.29 ± 0.02	0.76 ± 0.07
2-Co	2.0 ± 0.5	0.47 ± 0.01	0.97 ± 0.04
2-Ni	1.8 ± 0.5	0.42 ± 0.01	1.00 ± 0.05

ECSA = electrochemically active surface area ($C_{DoubleLayer}/C_{Specific}$); $\eta_{t=2h}$ = overpotential at t = 2 h, ε = Faradaic efficiency.

[a] Reference 9k;

[b] Reference 9i